High lithium conductivity in $Li_{1-2x}Ca_xSi_2N_3$

Eiichirou Narimatsu,[a] Yoshinobu Yamamoto, Takashi Takeda, Toshiyuki Nishimura, and Naoto Hirosaki
Nano-Ceramics Center, National Institute for Materials Science, Tsukuba, Ibaraki 305-0044, Japan

(Received 22 October 2010; accepted 4 February 2011)

Various compositions of $Li_{1-2x}Ca_xSi_2N_3$ ($x = 0$–0.2) were synthesized by the reaction of Li_3N, Si_3N_4, and Ca_3N_2 at temperatures of 1873–2073 K. Ca was incorporated into the $LiSi_2N_3$ host lattice to form a solid solution of $Li_{1-2x}Ca_xSi_2N_3$. The activation energy for ionic conduction was decreased and ionic conductivity at room temperature was enhanced by Ca doping. At 298 K, the ionic conductivity of densified $Li_{1-2x}Ca_xSi_2N_3$ ($x = 0.075$) ceramic reached 1.6×10^{-5} S m^{-1}, almost four orders of magnitude higher than that of densified $Li_{1-2x}Ca_xSi_2N_3$ ($x = 0$) ceramic (3.1×10^{-9} S m^{-1}). The change in the $LiSi_2N_3$ framework upon Ca doping decreased the interaction between the ions and increased the number of defects in the structure, making it easier for mobile Li^+ ions to migrate. Moreover, the incorporation of aliovalent substitutional Ca^{2+} ions in the $LiSi_2N_3$ lattice is expected to create Li^+ vacancies (V_{Li}) for charge compensation ($Li_{1-2x}Ca_xV_{Li}Si_2N_3$), thereby increasing the number of mobile Li^+ ions.

I. INTRODUCTION

All-solid-state lithium secondary batteries are required for new energy storage devices. The safety and reliability of batteries are greatly improved by avoiding the use of liquid electrolytes. Solid electrolytes with high lithium ion conductivity are essential for improving the performance of all-solid-state batteries. Among the binary and ternary lithium nitrides, Li_3N has the highest lithium ion conductivity of $\sim 10^{-3}$ Ω^{-1} cm^{-1}.[1] However, the decomposition voltage of Li_3N is rather low (0.44 V) at room temperature and decreases rapidly with increasing temperature.[1] Thus, the applicability of binary lithium nitride as a solid-state electrolyte at elevated temperatures is limited. To avoid this disadvantage, several ternary lithium nitrides have been investigated and their lithium ion conductivity has been measured.[2–6]

Ternary lithium silicon nitrides are examples of such interesting materials. Among the Li_3N–Si_3N_4 systems, there are several ternary compounds, including $LiSi_2N_3$,[4,7,8] Li_2SiN_2,[4,9,10] Li_5SiN_3,[4,11,12] $Li_{18}Si_3N_{10}$,[4] $Li_{21}Si_3N_{11}$,[4] and Li_8SiN_4.[4] Despite the crystal structure of some of these compounds remaining unclarified, the Li^+ ion conductivity of lithium silicon nitride compounds tends to increase with the Li/Si ratio.[4,13] Li_8SiN_4 has been reported to have the highest ionic conductivity among the above-mentioned ternary lithium nitrides.[4] However, it is unstable in the presence of moisture and soluble in water.[4]

Among the lithium silicon nitrides, $LiSi_2N_3$ is the most stable compound and has a well-defined wurtzite-type structure (space group $Cmc2_1$)[7,8] that is isostructural with Li_2SiO_3. The framework of $[Si_2N_3]^-$ in $LiSi_2N_3$ is built up of two-dimensional infinite parallel layers of condensed $[Si_6N_6]$ 12-membered rings formed by sharing the nitrogen atoms at the corners of the SiN_4 tetrahedra.[8] Li^+ occupies the 4a site and is directly connected with four and five nitrogen atoms within the unit cell (~2.3 Å) and the crossover unit cell (~2.7 Å), respectively. Regarding the practical use of the lithium silicon nitrides, $LiSi_2N_3$ is of particular interest because of its high stability. Therefore, we focused on $LiSi_2N_3$ in this study.

For the successful application of $LiSi_2N_3$ as a solid electrolyte in lithium ion batteries, the Li^+ ionic conductivity of $LiSi_2N_3$ must be increased. A large number of studies have focused on doping lithium ion–conductive solid electrolytes to improve their ionic conductivity.[14–23] In such studies, although the doped oxides were mainly investigated, a few studies on lithium ion conductivity in doped nitrides have also been reported. Lapp et al.[20] doped 1 at.% Mg, Cu, or Al into Li_3N, expecting to increase the number of Li vacancies for charge compensation. They reported negative results. Asai et al.[21] also investigated the effects of Cu substitution in Li_3N. They reported that the activation energy for Li^+ conduction was reduced by Cu substitution in Li_3N. In spite of this reduction, the ionic conductivity also decreased. These studies suggest that it is possible to improve the ionic conductivity of Li_3N through the reduction of the activation energy of diffusion by cation doping.

We explore chemical doping in $LiSi_2N_3$ with the aim of further improving the ionic conductivity. The radii of Li^+ and Ca^{2+} for octahedral coordination (CN6) are 0.76 and 1.00 Å, respectively.[24] Upon Ca doping, Ca^{2+} may substitute for the Li^+ ion of the $LiSi_2N_3$ structure. The host

[a]Address all correspondence to this author.
e-mail: NARIMATSU.Eiichirou@nims.go.jp
DOI: 10.1557/jmr.2011.50

 © Materials Research Society 2011

https://doi.org/10.1557/jmr.2011.50 Published online by Cambridge University Press

$LiSi_2N_3$ lattice expands with calcium doping, leading to much easier lithium ion diffusion. Furthermore, the substitution of Ca^{2+} for Li^+ is expected to create Li^+ vacancies for charge compensation, leading to increased Li^+ conductivity in $LiSi_2N_3$ solid electrolyte. The effects of Ca doping on the ionic conductivity of $LiSi_2N_3$ were investigated in this study. Furthermore, the ionic conductivity of Ca-doped $LiSi_2N_3$ is discussed in terms of its crystal structure.

II. EXPERIMENTAL

Undoped and Ca-doped $LiSi_2N_3$ ($Li_{1-2x}Ca_xSi_2N_3$) were prepared by the reaction of Li_3N (>99% purity; Kojundo Chemical Lab. Co., Ltd., Saitama, Japan), α-Si_3N_4 (SN-E10; UBE Industries, Ube, Japan), and Ca_3N_2 (Kojundo). Li_3N powder, α-Si_3N_4 powder, and Ca_3N_2 powder were mixed in silicon nitride mortar. Table I shows the compositions of the starting powders (x = 0–0.2) used in this study. The three powders were mixed in stoichiometric compositions. The mixed powder was placed in a 15-mm–diameter graphite die that was coated with BN powder to prevent the reaction between the powder and the die. All the processes were carried out in a nitrogen-filled glove box. Hot pressing was performed at 1873 or 2073 K for 10 min under a pressure of 30 MPa in a N_2 atmosphere (0.10 MPa).

The crystal structure of each sample was determined by powder x-ray diffraction (XRD, D8 ADVANCE; Bruker, Karlsruhe, Germany) using Cu Kα radiation. The densities and porosities of the samples were measured using Archimedes' method with distilled water as the immersion medium. The microstructures of the samples were observed by scanning electron microscopy (SEM, JSM-6700F; JEOL, Ltd., Tokyo, Japan). High-resolution transmission electron microscopy (HRTEM, JEM-4000EX; JEOL) was used to observe the grain boundaries. Composition analysis of the samples by energy-dispersive spectroscopy (EDS, JED-2300T; JEOL) in a device equipped with a field emission transmission electron microscope (FE-TEM, JEM-2100F; JEOL) was also performed.

Both sides of each sintered sample were polished to a 9-μm finish, and Au paste (Tanaka Kikinzoku, Tokyo, Japan) was applied to both sides of the sample by firing at 773 K for 30 min in N_2. Subsequently, a circular Pt electrode was attached to each side of the sample before it was mounted on the support tube in a ProboStat (NorECs AS, Oslo, Norway), measurement cell for electrochemical characterization (two-electrode measurements).[25,26] Relatively strong spring loads were applied with alumina parts to hold the assembly together and to maintain contact between the sample and the electrodes. Each sample was heated to the measurement temperature in dry nitrogen and then maintained at this temperature for 0.5 h before the measurement of complex impedance using a Solartron 1260 impedance analyzer (Solartron, Farnborough, UK) equipped with a Solartron 1296 dielectric interface (Solartron, Farnborough, UK). The measurement conditions were as follows: frequency range of 0.1 Hz–10 MHz, applied voltage for impedance measurement of 1 V, temperature range of 298–690 K, and flowing N_2 gas atmosphere.

Measurement of the direct current (DC) polarization was also carried out by a potentiostat/galvanostat device (VersaSTAT4; Princeton Applied Research, Oak Ridge, TN) to determine the electronic contribution to total conductivity of sintered sample using Au electrodes as blocking electrodes. A constant DC voltage of 1 V was applied to the hot-pressed samples at room temperature.

TABLE I. Compositions and sintering temperatures.

x in $Li_{1-2x}Ca_xSi_2N_3$	Composition of starting powder (wt%)			Sintering temperature (K)
	Si_3N_4	Li_3N	Ca_3N_2	
0	88.96	11.04	–	2073
0	88.96	11.04	–	1873
0.02	88.52	10.55	0.93	1873
0.05	87.86	9.82	2.32	1873
0.075	87.32	9.22	3.46	1873
0.1	86.79	8.62	4.59	1873
0.2	84.73	6.31	8.96	1873

III. RESULTS AND DISCUSSION

The compositions of the starting powders and the sintering temperatures of the as-hot-pressed $Li_{1-2x}Ca_xSi_2N_3$ materials (x = 0–0.2) are summarized in Table I. All materials were relatively stable in air at room temperature. The serial XRD patterns of $Li_{1-2x}Ca_xSi_2N_3$ (x = 0–0.2) sintered at 1873 and 2073 K are shown in Fig. 1. The XRD analysis indicates that $LiSi_2N_3$ is a primary phase in all materials except for $Li_{1-2x}Ca_xSi_2N_3$ (x = 0.2). A small amount of α-Si_3N_4 exists as a secondary phase in the case of x = 0.075. No other phase except for the primary $LiSi_2N_3$ phase and the secondary α-Si_3N_4 phase was detected by XRD analysis in the case of x = 0–0.075. On the other hand, large amounts of β-Si_3N_4 phase and α-Si_3N_4 phase and small amounts of unidentified phases were detected by XRD analysis in the case of x = 0.2. The diffraction patterns of the $Li_{1-2x}Ca_xSi_2N_3$ materials (x = 0–0.1) were similar to the JCPDS Power Diffraction File Card 01-076-0517 (International Centre for Diffraction Data, Newton Square, PA) for crystal $LiSi_2N_3$ [wurtzite-type structure (space group $Cmc2_1$)]. The lattice parameters and unit cell volume of each sample were obtained by fitting the powder XRD peak data using the $LiSi_2N_3$ crystal data[7] as an initial model and by using Jade 7 software (Rigaku, Tokyo, Japan). Figures 2(a) and 2(b) depict the variation of the lattice parameters and the unit cell volume of $Li_{1-2x}Ca_xSi_2N_3$ (x = 0–0.1) with increasing Ca^{2+} concentration, respectively. The lattice parameter a increased with increasing Ca^{2+} concentration. The lattice

https://doi.org/10.1557/jmr.2011.50 Published online by Cambridge University Press

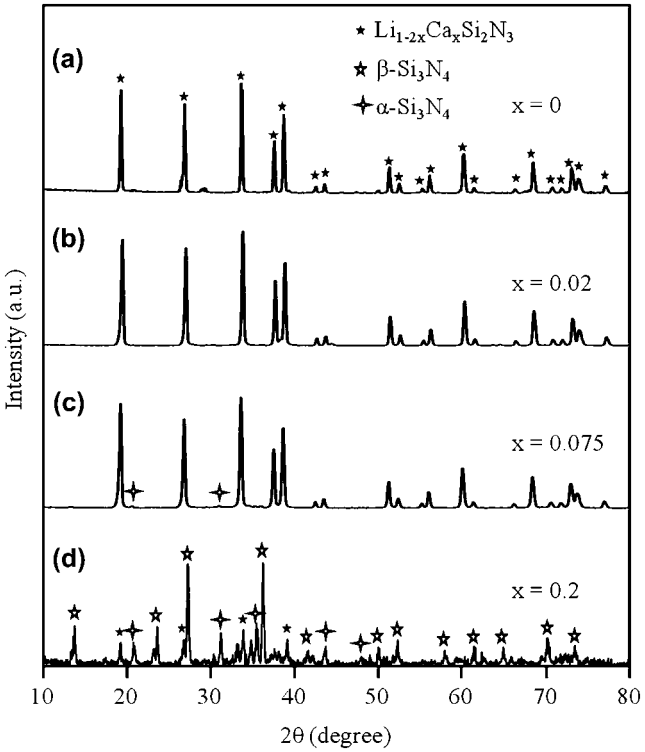


FIG. 1. X-ray diffraction patterns of $Li_{1-2x}Ca_xSi_2N_3$ (x = 0–0.2) sintered at (a) 2073 K and (b)–(d) 1873 K.

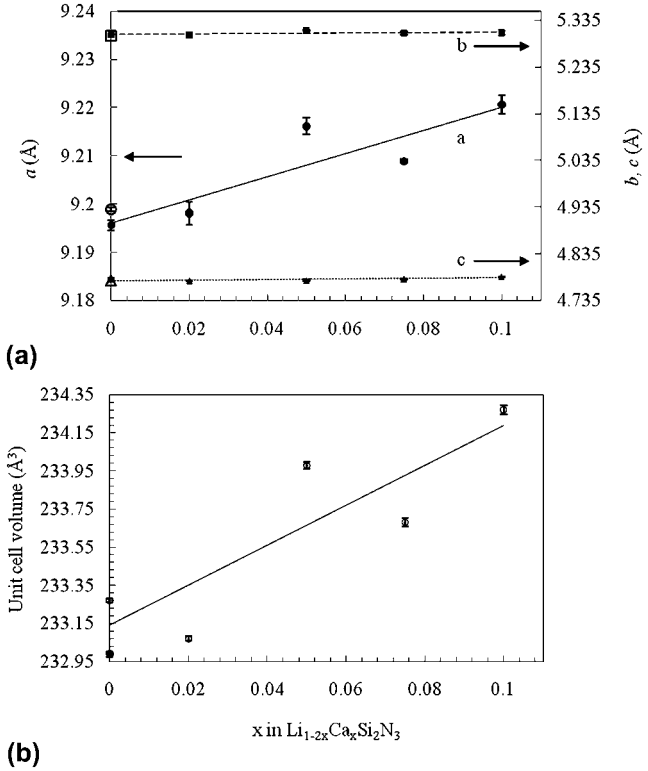


FIG. 2. (a) Lattice parameters of $Li_{1-2x}Ca_xSi_2N_3$ (x = 0–0.1) sintered at 1873 K [a (●), b (■), and c (▲)] and 2073 K [a (○), b (□), and c (△)] as functions of x, and (b) the unit cell volume for $Li_{1-2x}Ca_xSi_2N_3$ (x = 0–0.1) sintered at 1873 K (○) and 2073 K (●) as functions of x.

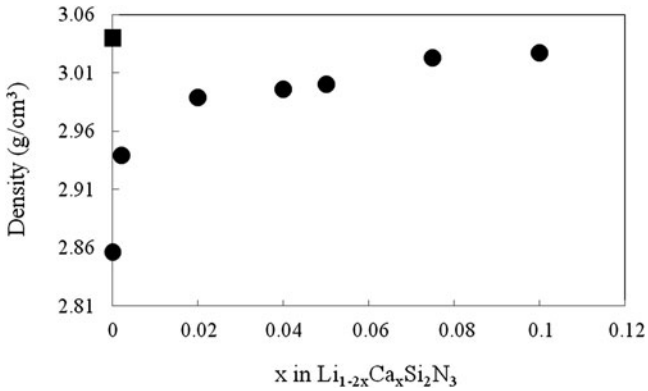


FIG. 3. Density of $Li_{1-2x}Ca_xSi_2N_3$ (x = 0–0.1) solid electrolytes sintered at 1873 K (●) and 2073 K (■) as a function of x.

is more rigid along the b-axis (b-axis lattice) and c-axis (c axis lattice) than along the a-axis (a-axis lattice) in $LiSi_2N_3$ because of the highly covalent Si–N bonds parallel to the b-axis and c-axis (along the Si–N layers). Thus, the incorporation of Ca^{2+} [ionic radius, 1.00 Å (coordination number CN = 6)] into the significant smaller crystallographic site of Li^+ [ionic radius, 0.76 Å (CN = 6)] in the host $LiSi_2N_3$ lattice resulted in the lattice parameter a being increased the most. The overall expansion of the lattice volume occurred by the incorporation of Ca^{2+} ions. The total change in lattice volume is ~0.4% from x = 0 to 0.1 [Fig. 2(b)]. Judging from the XRD patterns shown in Fig. 1 and the scattering data of the lattice parameters and volumes shown in Fig. 2, the solid solution range x appears to be 0–0.05. On the other hand, the lattice parameters and unit cell volume did not change with increasing sintering temperature in the case of $Li_{1-2x}Ca_xSi_2N_3$ (x = 0).

Figure 3 shows the variation of the density of $Li_{1-2x}Ca_xSi_2N_3$ (x = 0–0.1) with increasing Ca^{2+} concentration. The results illustrate that highly dense $Li_{1-2x}Ca_xSi_2N_3$ ceramics can be obtained by Ca doping at 1873 K. Density increased with increasing Ca^{2+} concentration. The density of $Li_{1-2x}Ca_xSi_2N_3$ (x = 0.075) sintered at 1873 K and $Li_{1-2x}Ca_xSi_2N_3$ (x = 0) sintered at 2073 K was almost the same. These results indicate that Ca doping promotes the densification of $LiSi_2N_3$. The porosity of $Li_{1-2x}Ca_xSi_2N_3$ (x = 0.075) sintered at 1873 K and $Li_{1-2x}Ca_xSi_2N_3$ (x = 0) sintered at 2073 K was ~1%.

The microstructures of the as-hot-pressed materials are shown in Fig. 4. No abnormal grain growth was observed, and the grains had an almost equiaxed form and were ~0.5–1 μm in diameter. The absence of residual porosity in the SEM images of all materials indicates that they were almost fully densified.

To investigate the grain boundary chemistry in detail, HRTEM was used. Figure 5 shows transmission electron microscopy (TEM) images of a grain boundary in the

https://doi.org/10.1557/jmr.2011.50 Published online by Cambridge University Press

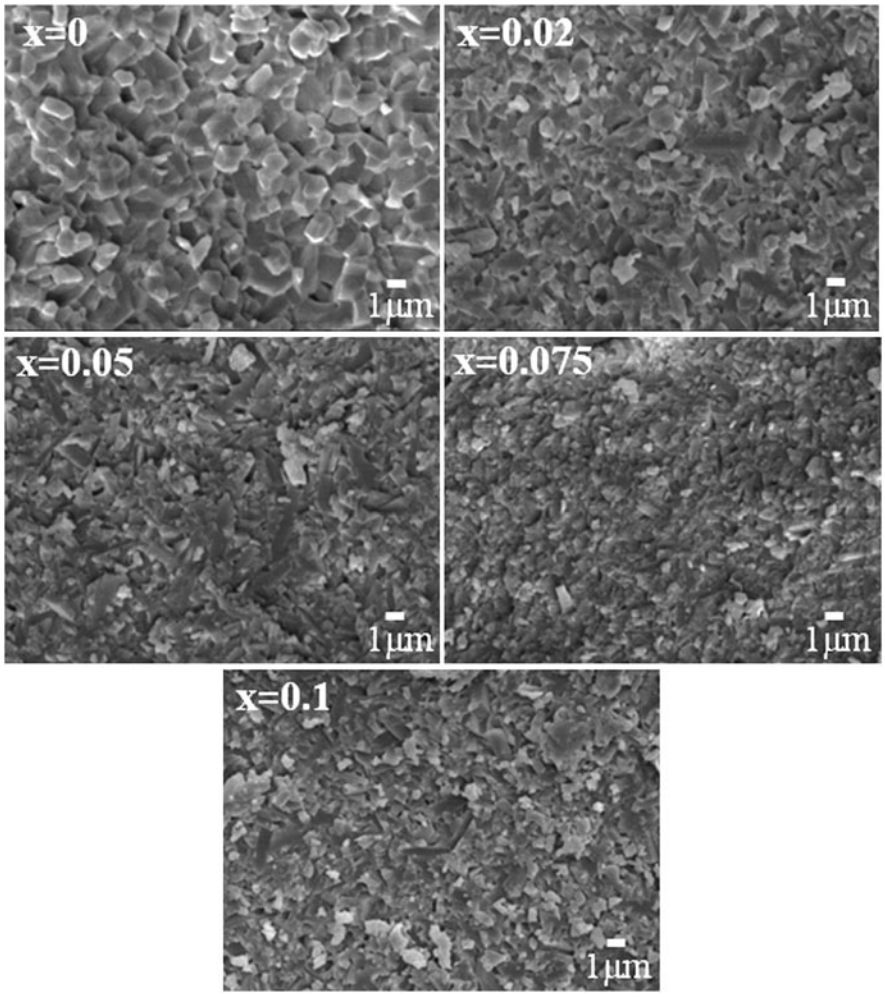


FIG. 4. Scanning electron microscopy images of fracture surface of sintered bodies of $Li_{1-2x}Ca_xSi_2N_3$ (x = 0–0.1) solid electrolytes sintered at 1873 K.

dense $Li_{1-2x}Ca_xSi_2N_3$ ceramic (x = 0, sintered at 2073 K) and the dense $Li_{1-2x}Ca_xSi_2N_3$ ceramic (x = 0.075, sintered at 1873 K). The high-magnification images of both materials revealed that an intergranular glassy film existed at grain boundaries. The thicknesses of this film in dense $Li_{1-2x}Ca_xSi_2N_3$ (x = 0, sintered at 2073 K) and dense $Li_{1-2x}Ca_xSi_2N_3$ (x = 0.075, sintered at 1873 K) were almost 5 and 2 nm, respectively. This indicates that the thickness of the intergranular glassy film tended to decrease with Ca doping. Because Ca^{2+} is known to be a potent silica network modifier, causing a decrease in viscosity of several orders, it is expected that the addition of Ca^{2+} will decrease the steric repulsive force between grains and cause a reduction in the film thickness.[27] The decreasing thickness of the amorphous grain boundary layer with Ca^{2+} doping also suggests that Ca additives increase the oxygen content in the $LiSi_2N_3$ grains.

EDS point elemental analysis using an FE-TEM with a focused electron beam size of ~1 nm was performed to examine the distribution of dopant Ca^{2+} cations in dense $Li_{1-2x}Ca_xSi_2N_3$ (x = 0, sintered at 2073 K) and dense $Li_{1-2x}Ca_xSi_2N_3$ (x = 0.075, sintered at 1873 K). The spatial resolution available using the FE-TEM in this study was ~2–3 nm. The results of TEM-EDS analysis for dense

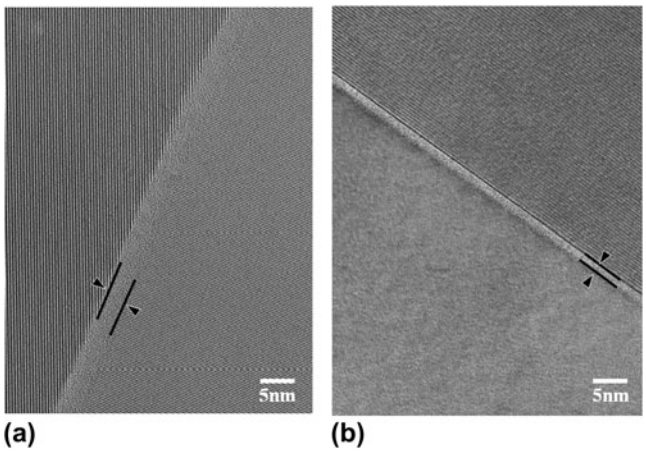


FIG. 5. High-resolution transmission electron microscopy image of a grain boundary in (a) $Li_{1-2x}Ca_xSi_2N_3$ (x = 0, sintered at 2073 K) and (b) $Li_{1-2x}Ca_xSi_2N_3$ (x = 0.075, sintered at 1873 K).

https://doi.org/10.1557/jmr.2011.50 Published online by Cambridge University Press

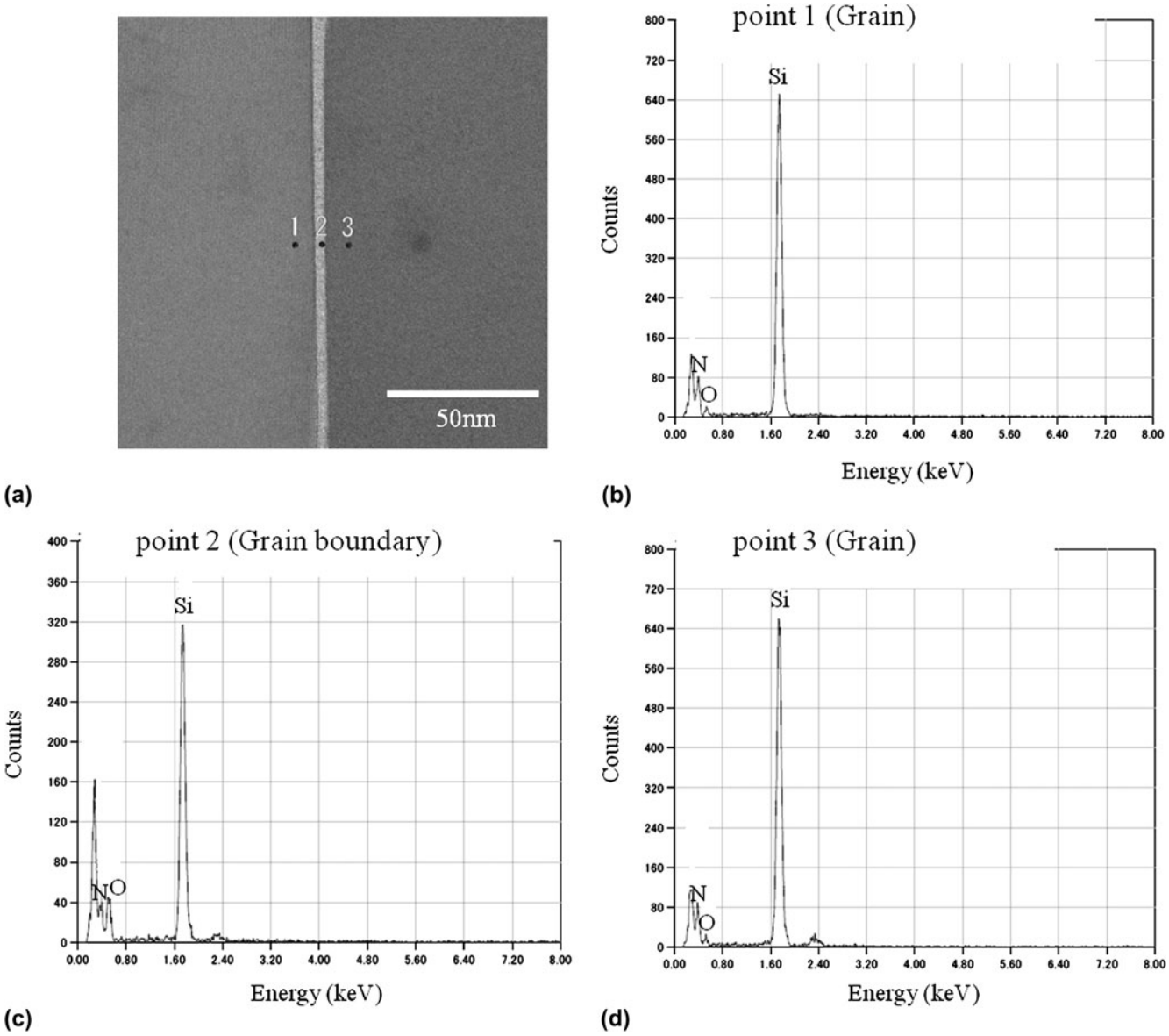


FIG. 6. (a) Transmission electron microscopy (TEM) image of grains and grain boundary in the $Li_{1-2x}Ca_xSi_2N_3$ ceramic ($x = 0$, sintered at 2073 K), and energy-dispersive spectroscopy (EDS) for (b) point 1 (grain), (c) point 2 (grain boundary), and (d) point 3 (grain).

$Li_{1-2x}Ca_xSi_2N_3$ ($x = 0$, sintered at 2073 K) and dense $Li_{1-2x}Ca_xSi_2N_3$ ($x = 0.075$, sintered at 1873 K) are shown in Figs. 6 and 7, respectively. The peak at ~0.3 keV observed in Figs. 6 and 7 is a carbon peak due to the carbon coating on the samples used to prevent charging. The carbon peak intensity changes with the amount of the carbon and sample thickness. The EDS analysis indicates that elemental Si, O, and N are present in the grain boundary glassy phase, and by comparing the three EDS plots shown in Figs. 6(b)–6(d) for points 1, 2, and 3, respectively, it can be seen that the oxygen concentrates in the grain boundary regions. These results indicate that a silicate-based Si–O–N glassy phase was formed at the grain boundaries of $Li_{1-2x}Ca_xSi_2N_3$ ($x = 0$, sintered at 2073 K). The oxygen probably originates from the raw Si_3N_4 powder because it contained oxygen, which mainly existed as SiO_2 on the surface of the powder.[28,29] The oxygen in $LiSi_2N_3$ might also originate from the Li_3N powder.

In Fig. 7, the EDS spectra for points 4 and 5 were omitted, because they were similar to those for points 2 and 1, respectively. By comparing the three EDS plots shown in Figs. 7(b)–7(d) for points 1–3, respectively, it can be seen that Ca and O exist with a high concentration at the grain boundaries (point 3) of $Li_{1-2x}Ca_xSi_2N_3$ ($x = 0.075$). The EDS analysis indicates that elemental Ca, Si, O, and N are present in the grain boundary glassy phase. These results indicate that a silicate-based Ca–Si–O–N glassy phase was formed at grain boundaries of $Li_{1-2x}Ca_xSi_2N_3$ ($x = 0.075$,

https://doi.org/10.1557/jmr.2011.50 Published online by Cambridge University Press

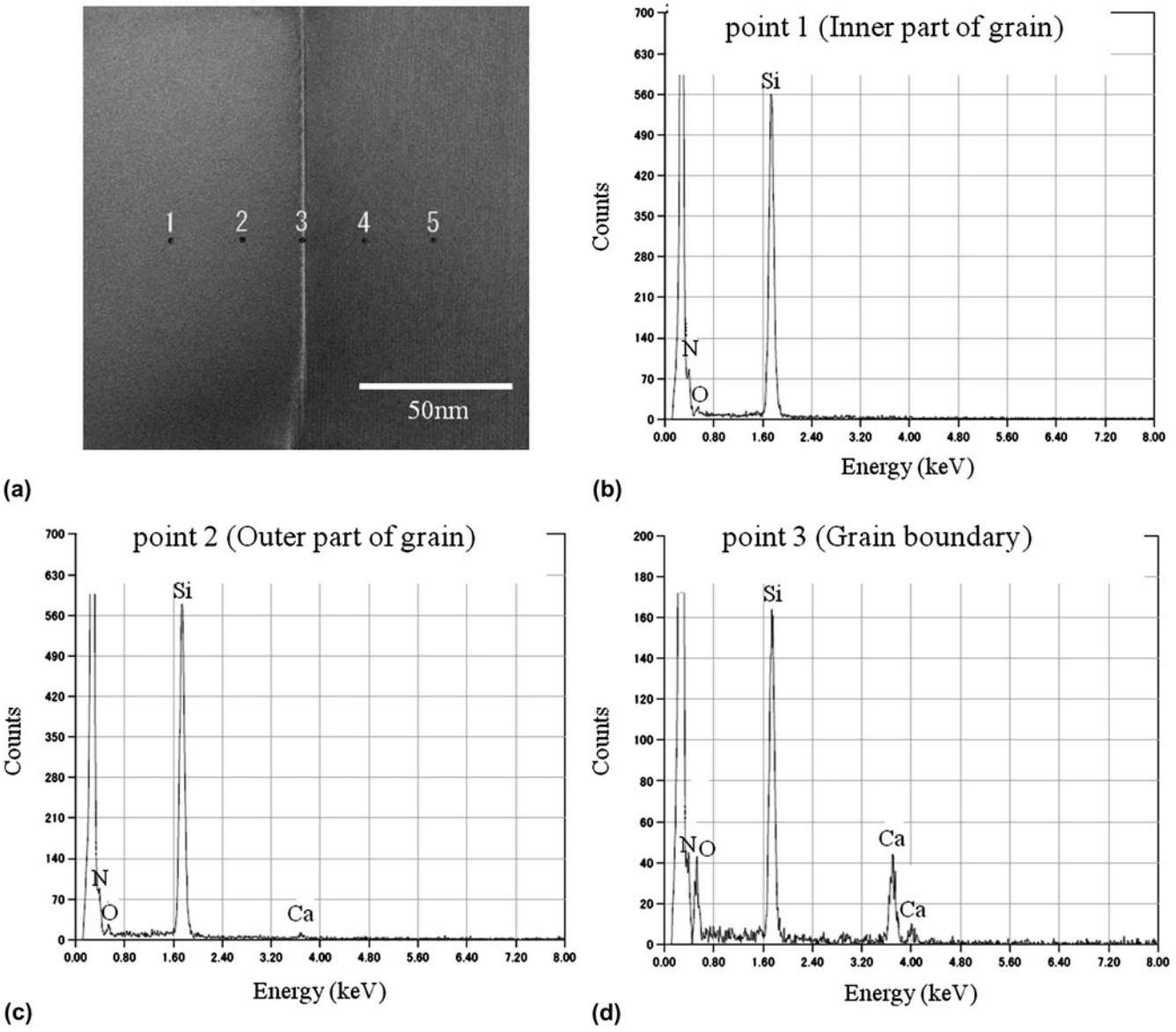


FIG. 7. (a) TEM micrograph of grains and grain boundary in the $Li_{1-2x}Ca_xSi_2N_3$ ceramic ($x = 0.075$, sintered at 1873 K) and EDS spectra for (b) point 1 (inner part of grain), (c) point 2 (outer part of grain), and (d) point 3 (grain boundary).

sintered at 1873 K). In this case, not only Si_3N_4 and Li_3N but also Ca_3N_2 may be an oxygen source for $Li_{1-2x}Ca_xSi_2N_3$. Figure 7 clearly shows that most of the Ca added in the starting materials precipitates at the amorphous grain boundaries, indicating that the solid solution limit x for $Li_{1-2x}Ca_xSi_2N_3$ is far from $x = 0.075$.

The EDS analysis also indicates that Ca^{2+} is present in the grain interior (point 2). This suggests that Ca^{2+} is incorporated into the $LiSi_2N_3$ host lattice. The calcium content for the inner part of the grain (point 1) was lower than that for the outer part (point 2). These results indicate that the chemical compositions of the inner and outer parts of $Li_{1-2x}Ca_xSi_2N_3$ grains are different, with Ca cations existing in a higher concentration at the outer part of $Li_{1-2x}Ca_xSi_2N_3$ grains. No Ca peak is observed at the inner part of the grain (point 1) [Fig. 7(b)]. The detection limit of Ca in the EDS analysis is ~1 wt% (10,000 ppm) in this study; thus, the calcium content for the inner part of the grain (point 1) must be lower than 1 wt% (10,000 ppm).

The complex impedance was measured to determine the conductivity. In general, the alternating current impedance of an ionic conductor measured by a two-probe method contains contributions from the grain interior, the grain boundaries, and the electrode–electrolyte interface, which can be illustrated in the complex plane by three successive arcs.[30,31] The arc at the high-frequency end of the spectrum represents the grain-interior resistivity, that at the middle of the spectrum is a consequence of the

https://doi.org/10.1557/jmr.2011.50 Published online by Cambridge University Press

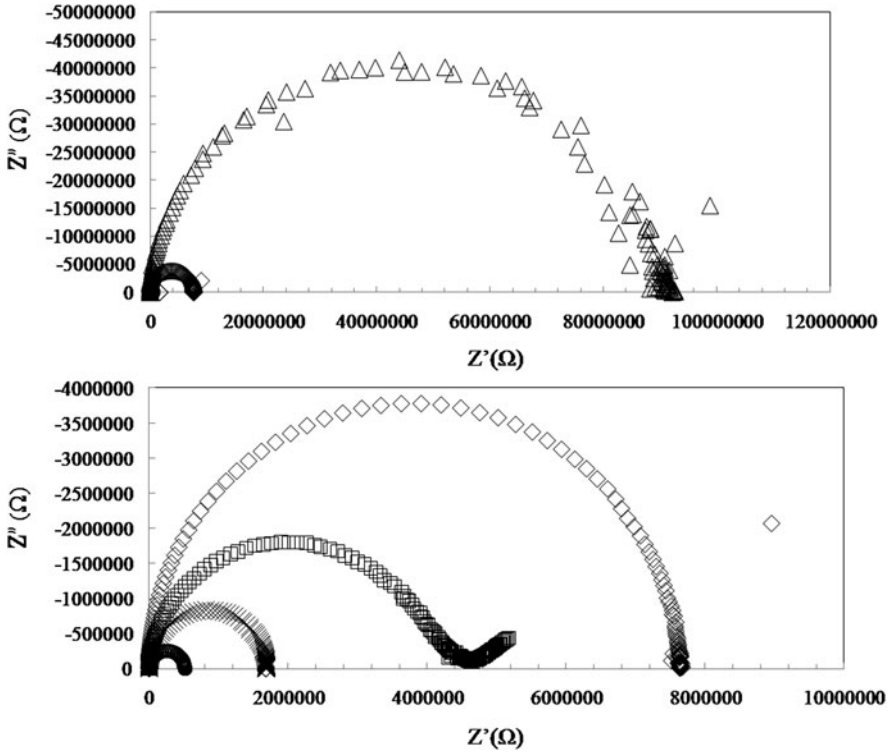


FIG. 8. Impedance spectra (recorded at 490 K in N_2) of $Li_{1-2x}Ca_xSi_2N_3$ [$x = 0$ (□), $x = 0.02$ (△), $x = 0.05$ (◇), and $x = 0.075$ (○)] sintered at 1873 K and $Li_{1-2x}Ca_xSi_2N_3$ [$x = 0$ (×)] sintered at 2073 K.

grain-boundary effect, and the low-frequency arc is assigned to the electrode response. In practice, however, not all these arcs can be observed, depending on the nature of the sample and the measurement conditions.

Figure 8 shows typical complex impedance diagrams for $Li_{1-2x}Ca_xSi_2N_3$ ($x = 0$–0.075, sintered at 1873 K) and $Li_{1-2x}Ca_xSi_2N_3$ ($x = 0$, sintered at 2073 K) recorded at 490 K in N_2. One semicircular arc was observed for all materials. The shape of the arc changes with the concentration of calcium (x) in $Li_{1-2x}Ca_xSi_2N_3$. In this context, the semicircular arc is attributed to $Li_{1-2x}Ca_xSi_2N_3$ grains and grain boundaries. The total conductivity of each sample was estimated from the intersections between the extrapolated semicircular arc and the real axis.

Figure 9 shows the time dependence of DC current at room temperature for $Li_{1-2x}Ca_xSi_2N_3$ ($x = 0$–0.075, sintered at 1873 K) and $Li_{1-2x}Ca_xSi_2N_3$ ($x = 0$, sintered at 2073 K) ceramics. A constant voltage of 1 V was applied to these ceramics for 1800 s using Au-blocking electrodes to determine the electronic contribution. These ceramics were initially polarized and then the current was drastically decreased within a very short time. The steady current after polarization could not be determined clearly because the current was too small to be measured by the potentiostat/galvanostat device used in this study. These results indicates that the electronic conductivities of $Li_{1-2x}Ca_xSi_2N_3$ ($x = 0$, 2073 K sintered) ceramics and $Li_{1-2x}Ca_xSi_2N_3$ ($x = 0$–0.075, 1873 K sintered) ceramics were negligibly small. Moreover, Yamane et al.[4] reported that the electronic conductivity of $LiSi_2N_3$ was less than 1% of the total conductivity at temperatures between 423 and 673 K. The experimental conditions of their study were almost the same as in this study. In addition, the mobility of calcium ions is generally negligibly small.[32] Thus, we believe that most of the conductivity of the $Li_{1-2x}Ca_xSi_2N_3$ ($x = 0$–0.075) materials obtained in this study is caused by the migration of lithium ions.

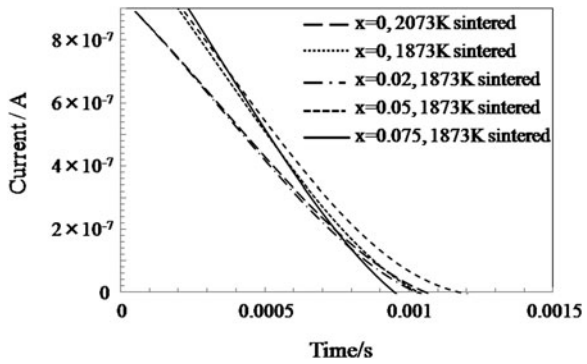


FIG. 9. Charge in current relative to time after applying a constant direct current voltage of 1 V to the $Li_{1-2x}Ca_xSi_2N_3$ ceramic ($x = 0$–0.075, sintered at 1873 K) and the $Li_{1-2x}Ca_xSi_2N_3$ ceramic ($x = 0$, sintered at 2073 K).

https://doi.org/10.1557/jmr.2011.50 Published online by Cambridge University Press

Figure 10 shows the temperature dependences of the ionic conductivity for all the $Li_{1-2x}Ca_xSi_2N_3$ (x = 0–0.075) materials considered in this study. As shown in Fig. 10, the plots of $\ln(\sigma T)$ against $1000/T$ were found to be linear and to closely fit the Arrhenius equation $\sigma T = A \exp(-E_a/RT)$, where A is the pre-exponential factor, E_a is the activation energy for conduction, and R is the gas constant. Table II summarizes the conductivities at room temperature (298 K) and the activation energies of conduction. The conductivities at 298 K for $Li_{1-2x}Ca_xSi_2N_3$ (x = 0, sintered at 2073 K) and $Li_{1-2x}Ca_xSi_2N_3$ (x = 0–0.02, sintered at 1873 K) were estimated by extrapolating the lines representing conductivity in Fig. 10 to 298 K. The conductivities at room temperature of samples with x = 0.1 and 0.2 were smaller than that of the sample with x = 0.075. This reduction in conductivity may have been caused by the impurity phases as shown in Fig. 1(d).

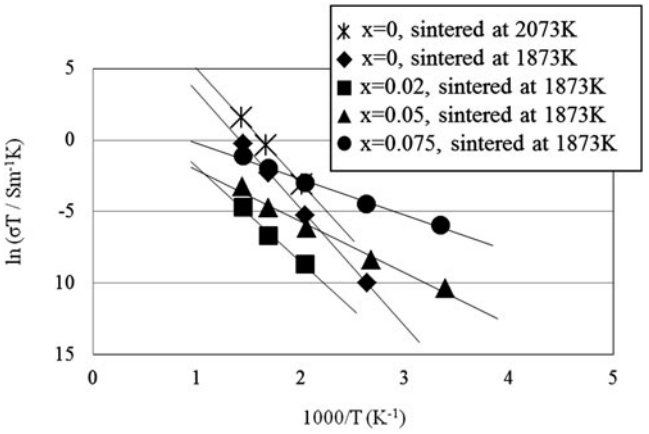


FIG. 10. Temperature dependences of ionic conductivities of $Li_{1-2x}Ca_xSi_2N_3$ (x = 0, sintered at 2073 K) and $Li_{1-2x}Ca_xSi_2N_3$ (x = 0–0.075, sintered at 1873 K).

TABLE II. Ionic conductivities and activation energies of $Li_{1-2x}Ca_xSi_2N_3$ (x = 0–0.075).

x in $Li_{1-2x}Ca_xSi_2N_3$	Sintering temperature (K)	σ (S m^{-1}) (298 K)	E_a (kJ mol^{-1})
0	2073	3.1×10^{-9}	67
0	1873	3.9×10^{-10}	68
0.02	1873	1.9×10^{-9}	55
0.05	1873	9.1×10^{-7}	30
0.075	1873	1.6×10^{-5}	21

The ionic conductivity increased with increasing sintering temperature and material density, as shown by the results for $Li_{1-2x}Ca_xSi_2N_3$ (x = 0, sintered at 1873 K) and $Li_{1-2x}Ca_xSi_2N_3$ (x = 0, sintered at 2073 K). The high ionic conductivity of $Li_{1-2x}Ca_xSi_2N_3$ (x = 0, sintered at 2073 K) may have been caused by the increased density of the sintered sample, which enhances grain boundary conductivity. However, the activation energy for conduction hardly changed with increasing sintering temperature and material density. On the other hand, the activation energy for conduction gradually decreased with increasing Ca content. Upon increasing the amount of Ca (x) in $Li_{1-2x}Ca_xSi_2N_3$ from x = 0 to 0.075, the activation energy decreased from 67 to 21 kJ/mol. The decrease in activation energy caused the enhancement of ionic conductivity at room temperature. At 298 K, the ionic conductivity of densified $Li_{1-2x}Ca_xSi_2N_3$ (x = 0.075, sintered at 1873 K) ceramic was 1.6×10^{-5} S m^{-1}, almost four orders of magnitude higher than that of the densified $Li_{1-2x}Ca_xSi_2N_3$ ceramic (x = 0, sintered at 2073 K) of 3.1×10^{-9} S m^{-1}. The decrease in activation energy and the enhancement of ionic conductivity at room temperature are caused by the incorporation of Ca^{2+} into the host $LiSi_2N_3$ lattice. As mentioned earlier, the lattice parameter a and the unit cell volume increased with increasing Ca^{2+} concentration. Thus, the framework of $LiSi_2N_3$ becomes less rigid [Fig. 11(a)].

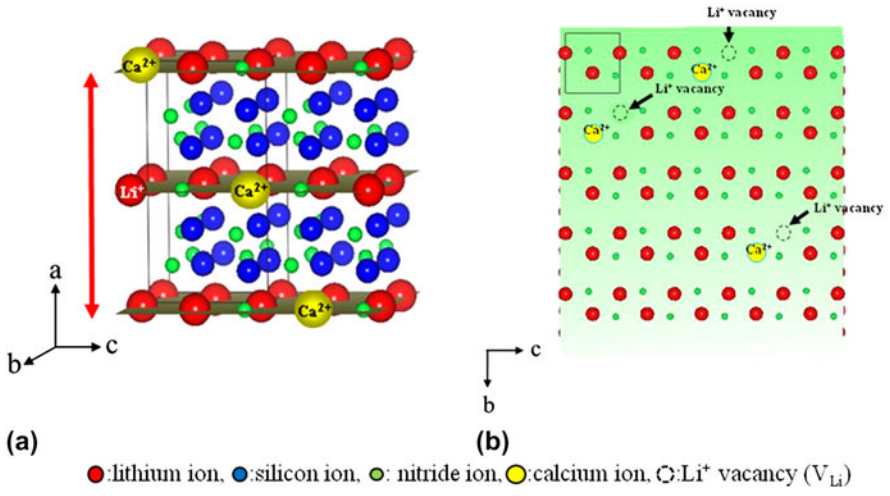


FIG. 11. Schematic illustration of changes occurring in the $LiSi_2N_3$ crystal structure upon doping Ca^{2+} cations: (a) the framework of $LiSi_2N_3$ becomes less rigid and (b) Li^+ vacancies (V_{Li}) are created for charge compensation.

https://doi.org/10.1557/jmr.2011.50 Published online by Cambridge University Press

This decreases the interaction between the ions and increases the number of defects in the structure. This increases the Li^+ mobility. In addition, the incorporation of aliovalent substitutional Ca^{2+} ions in the $LiSi_2N_3$ lattice is expected to create Li^+ vacancies (V_{Li}) for charge compensation ($Li_{1-2x}Ca_xV_{Li}Si_2N_3$), thereby increasing the Li^+ mobility [Fig. 11(b)]. The decrease in the thickness of the amorphous grain boundary layer upon Ca doping shown in Fig. 5 also suggests that Ca^{2+} ions increase the oxygen content in the $LiSi_2N_3$ grains. O^{2-} may substitute for N^{3-} in the $LiSi_2N_3$ structure. The substitution of O^{2-} for N^{3-} is expected to create Li^+ vacancies for charge compensation, leading to increased Li^+ conductivity in the $LiSi_2N_3$ grains.

Although lithium could not be detected by EDS, we cannot rule out the possibility that the change in the grain boundary structure upon Ca doping might change the grain boundary conductivity and the total conductivity. The decrease in grain boundary thickness due to Ca doping shortens the length of Li pathways between grains, thereby making it easier for Li^+ ions to migrate between grains.

IV. CONCLUSIONS

In this study, the effect of Ca doping on the ionic conductivity of $LiSi_2N_3$ ($Li_{1-2x}Ca_xSi_2N_3$) was studied. The incorporation of Ca^{2+} into the significantly smaller crystallographic site of Li^+ in the host $LiSi_2N_3$ lattice increased the lattice parameter a. The change in the total lattice volume was ~0.4% from $x = 0$ to 0.1. TEM-EDS results indicated that a silicate-based Ca–Si–O–N glassy phase was formed at the grain boundaries of $Li_{1-2x}Ca_xSi_2N_3$ ($x = 0.075$, sintered at 1873 K). The activation energy for Li ionic conduction gradually decreased with increasing Ca content. Upon increasing the amount of Ca (x) in $Li_{1-2x}Ca_xSi_2N_3$ from 0 to 0.075, the activation energy decreased from 67 to 21 kJ/mol. At 298 K, the ionic conductivity of densified $Li_{1-2x}Ca_xSi_2N_3$ ($x = 0.075$, sintered at 1873 K) ceramic reached 1.6×10^{-5} S m^{-1}, almost four orders of magnitude higher than that of densified $Li_{1-2x}Ca_xSi_2N_3$ ($x = 0$, sintered at 2073 K) ceramic (3.1×10^{-9} S m^{-1}).

REFERENCES

1. A. Rabenau: Lithium nitride and related materials case study of the use of modern solid state research techniques. *Solid State Ion* **6**, 277 (1982).
2. H. Yamane, S. Kikkawa, and M. Koizumi: High- and low-temperature phases of lithium boron nitride, Li_3BN_2: Preparation, phase relation, crystal structure, and ionic conductivity. *J. Solid State Chem.* **71**, 1 (1987).
3. H. Yamane, S. Kikkawa, and M. Koizumi: Lithium aluminum nitride, Li_3AlN_2 as a lithium solid electrolyte. *Solid State Ion* **15**, 51 (1985).
4. H. Yamane, S. Kikkawa, and M. Koizumi: Preparation of lithium silicon nitrides and their lithium ion conductivity. *Solid State Ion* **25**, 183 (1987).
5. P. Hartwig, W. Weppner, and W. Wichelhaus: Fast ionic lithium conduction in solid lithium nitride chloride. *Mater. Res. Bull.* **14**, 493 (1979).
6. W. Weppner, P. Hartwig, and A. Rabenau: Consideration of lithium nitride halides as solid electrolytes in practical galvanic cell applications. *J. Power Sources* **6**, 251 (1981).
7. J. David, Y. Laurent, J.P. Charlot, and J. Lang: Etude cristallographique d'un nitrure I 4_2 5_3. La structure tetraedrique type wurtzite de $LiSi_2N_3$. *Bull. Soc. Fr. Mineral Crystallogr.* **96**, 21 (1973).
8. M. Orth and W. Schnick: Zur Kenntnis von $LiSi_2N_3$: Synthese und Verfeinerung der Kristallstruktur. *Z. Anorg. Allg. Chem.* **625**, 1426 (1999).
9. A.J. Anderson, R.G. Blair, S.M. Hick, and R.B. Kaner: Microwave initiated solid-state metathesis routes to Li_2SiN_2. *J. Mater. Chem.* **16**, 1318 (2006).
10. M.S. Bhamra and D.J. Fray: The electrochemical properties of Li_3AlN_2 and Li_2SiN_2. *J. Mater. Sci.* **30**, 5381 (1995).
11. R. Juza, H.H. Weber, and E. Meyer-Simon: Uber ternare Nitride und Oxonitride von Elementen der 4. Gruppe. *Z. Anorg. Allg. Chem.* **273**, 48 (1953).
12. A.T. Dadd and P. Hubberstey: Solutions of lithium salts in liquid lithium: Interaction between silicon and nitrogen to form the ternary compound, Li_5SiN_3. *J. Chem. Soc. Dalton Trans.*2175 (1982).
13. V. Ischenko, L. Kienle, and M. Jansen: Formation and structure of $LiSi_2N_3$-AlN solid solutions. *J. Mater. Sci.* **37**, 5305 (2002).
14. X. Wu, Z. Wen, X. Xu, and J. Han: Synthesis and ionic conductivity of Mg-doped Li_2TiO_3. *Solid State Ion* **179**, 1779 (2008).
15. F. Bennani and E. Husson: Impedance spectroscopy analysis of pure and Ni-doped lithium tantalite. *J. Eur. Ceram. Soc.* **21**, 847 (2001).
16. R. Kanno, Y. Takeda, K. Takada, and O. Yamamoto: Ionic conductivity and phase transition of the spinel system $Li_{2-2x}M_{1+x}Cl_4$ (M = Mg, Mn, Cd). *J. Electrochem. Soc.* **131**, 469 (1984).
17. V. Thangadurai and W. Weppner: Effect of sintering on the ionic conductivity of garnet-related structure $Li_5La_3Nb_2O_{12}$ and In- and K-doped $Li_5La_3Nb_2O_{12}$. *J. Solid State Chem.* **179**, 974 (2006).
18. H.-T. Chung, J.-G. Kim, and H.-G. Kim: Dependence of the lithium ionic conductivity on the B-site ion substitution in $(Li_{0.5}La_{0.5})Ti_{1-x}M_xO_3$ (M = Sn, Zr, Mn, Ge). *Solid State Ion* **107**, 153 (1998).
19. A. Belous, E. Pashkova, O. Gavrilenko, O. V'yunov, and L. Kovalenko: Solid electrolytes based on lithium-containing lanthanum metaniobates. *J. Eur. Ceram. Soc.* **24**, 1301 (2004).
20. T. Lapp, S. Skaarup, and A. Hooper: Ionic conductivity of pure and doped Li_3N. *Solid State Ion* **11**, 97 (1983).
21. T. Asai, K. Nishida, and S. Kawai: Synthesis and ionic conductivity of $Cu_xLi_{3-x}N$. *Mater. Res. Bull.* **19**, 1377 (1984).
22. A. Mei, X.-L. Wang, Y.-C. Feng, S.-J. Zhao, G.-J. Li, H.-X. Geng, Y.-H. Lin, and C.-W. Nan: Enhanced ionic transport in lithium lanthanum titanium oxide solid state electrolyte by introducing silica. *Solid State Ion* **179**, 2255 (2008).
23. A. Mei, X.-L. Wang, J.-L. Lan, Y.-C. Feng, H.-X. Geng, Y.-H. Lin, and C.-W. Nan: Role of amorphous boundary layer in enhancing ionic conductivity of lithium-lanthanum-titanate electrolyte. *Electrochim. Acta* **55**, 2958 (2010).
24. R.D. Shannon: Revised effective ionic radii and systematic studies of interatomic distances in halides and chalcogenides. *Acta Crystallogr.* **A32**, 751 (1976).
25. P.I. Dahl, R. Haugsrud, H.L. Lein, T. Grande, T. Norby, and M. Einarsrud: Synthesis, densification and electrical properties of strontium cerate ceramics. *J. Eur. Ceram. Soc.* **27**, 4461 (2007).
26. T. Norby and M. Hartmanova: Electrical conductivity and ionic transport number of YSZ and Cr-doped YSZ single crystals at 200–1000°C. *Solid State Ion* **67**, 57 (1993).
27. I. Tanaka, H.-J. Kleebe, M.K. Cinibulk, J. Bruley, D.-R. Clarke, and M. Ruhle: Calcium concentration dependence of the intergranular

https://doi.org/10.1557/jmr.2011.50 Published online by Cambridge University Press

film thickness in silicon nitride. *J. Am. Ceram. Soc.* **77**(4), 911 (1994).
28. P. Greil, R. Nitzsche, H. Friedrich, and W. Hermel: Evaluation of oxygen content on silicon nitride powder surface from the measurement of the isoelectric point. *J. Eur. Ceram. Soc.* **7**, 353 (1991).
29. J. Bermudo, M.I. Osendi, and J.L.G. Fierro: Oxygen distribution in AlN and Si_3N_4 powders as revealed by chemical and spectroscopy techniques. *Ceram. Int.* **26**, 141 (2000).
30. Y. Li, M. Liu, J. Gong, Y. Chen, Z. Tang, and Z. Zhang: Grain-boundary effect in zirconia stabilized with yttria and calcia by electrical measurements. *Mater. Sci. Eng. B* **103**, 108 (2003).
31. T.S. Zhan, J. Ma, Y.Z. Chen, L.H. Luo, L.B. Kong, and S.H. Chan: Different conduction behaviors of grain boundaries in SiO_2-containing 8YSZ and CGO20 electrolytes. *Solid State Ion* **177**, 1227 (2006).
32. G. Gruener, D. De Sousa Meneses, P. Odier, and J.P. Loup: Influence of the network on conductivity in ternary CaO-Al_2O_3-SiO_2 glasses and melts. *J. Non Cryst. Solids* **281**, 117 (2001).

https://doi.org/10.1557/jmr.2011.50 Published online by Cambridge University Press